ORIGINAL PAPER

Superior conductivity and accelerated kinetics $Na_3V_2(PO_4)_2F_3$@CNTs with high performance for sodium-ion batteries

Haitao Tong[1] · **Haowei Han**[1] · **Guangying Zhang**[1] · **Kefu Gao**[1] · **Qingyu Dong**[2] · **Fangdong Hu**[1] · **Xiaolei Jiang**[1]

Abstract

$Na_3V_2(PO_4)_2F_3$ with a high theoretical energy density, robust 3D structure, and superior thermal stability has become one of the popular cathode materials for sodium ion batteries. Currently, its poor intrinsic electronic conductivity leads to unsatisfactory rate performance, which is still the bottleneck for commercializing sodium-ion batteries. In this work, carbon nanotube–intertwined $Na_3V_2(PO_4)_2F_3$ nanospheres (notated as NVPF@CNTs) are successfully synthesized by a solvothermal method and subsequent heat treatment. In NVPF@CNTs composites, the carbon nanotubes constituted a continuous conductive 3D carbon network, realizing the improvement of electrical conductivity. The NVPF nanospheres are exposed to the electrolyte to increase the contact area with the electrolyte and greatly shorten the diffusion distance of Na^+. The unique architecture endorses superior electrochemical performance and good reaction kinetics. Thus, the NVPF@CNTs as cathode exhibits good cycling performance (117.6 mAh g^{-1} at 0.2 C after 300 cycles) and rate capability (73.4 mAh g^{-1} at 5 C with a high capacity retention ratio of 91.6% after 600 cycles). The excellent electrochemical performance for NVPF@CNTs opens up a new way to achieve high performance of sodium-ion batteries.

Keywords Superior conductivity · Accelerated kinetics · Carbon nanotubes · Electrochemical performance · Sodium-ion batteries

Introduction

As the next generation of large-scale energy storage batteries with important application prospects, sodium-ion batteries (SIBs) have attracted great attention due to their advantages of abundant resources, wide distribution, low price, and similar working voltage with lithium-ion batteries [1–3]. However, the practical process of SIBs still faces many challenges, such as low energy and power density, short cycle life, and low temperature performance. Restricted by the storage mechanism of insertion/extraction, limited number of (de-)sodiation, and heavy element composition, the cathode material has a lower theoretical specific capacity compared with the anode material, thus becoming one of the key parts to restrict the development of SIBs [4–7]. Among cathode materials, $Na_3V_2(PO_4)_2F_3$ (marked as NVPF) has attracted extensive attention of scientists in recent years due to the advantages of stable structure, good thermal stability, and high charge/discharge plateaus, etc. [8–10]. Unfortunately, its poor intrinsic electronic conductivity (just 10^{-12} S cm^{-1}) often leads to unsatisfactory rate performance. To solve this problem, carbon modification is an effective solution. Carbon materials, such as amorphous carbon, graphene, and other carbonaceous materials, not only can effectively prevent the agglomeration of NVPF nanoparticles, but also buffer the volume change during the (de)intercalation processes of Na^+, ensuring the stability of NVPF structure [11–14]. Moreover, it can make the co-diffusion between electrons and ions fast, and reduce the charge transfer impedance between the interface and electrolyte.

Among them, compositing NVPF with carbon nanotubes (CNTs) is regarded as an effective way to improve the electrochemical performance because of high conductivity and good thermal stability of CNTs [4]. Zhanliang Tao et al.

✉ Fangdong Hu
hufangdong@lyu.edu.cn

✉ Xiaolei Jiang
jiangxiaolei@lyu.edu.cn

[1] School of Chemistry and Chemical Engineering, Linyi University, Linyi 276005, People's Republic of China

[2] CAS Center for Excellence in Nanoscience, Suzhou Institute of Nano-Tech and Nano-Bionics, Chinese Academy of Sciences, Suzhou 215123, People's Republic of China

synthesized NVPF-SWCNT by a solvothermal method, which exhibited a high reversible capacity of 117 mAh g^{-1} at rate of 0.5 C in non-aqueous electrolyte [15]. Hou and Wu et al. prepared tetragonal NVPF@C particles connected by CNTs [16]. The three-dimensional conductive network, which was caused by the CNTs and nano-carbon coating layer, showed excellent electrochemical performance.

In the present work, we proposed a solvothermal method and subsequent heat treatment to construct a 3D composite structure of CNT-intertwined NVPF nanospheres. This unique architecture offers a stable framework for fast transmission of Na$^+$ and reduction of the volume variations during charge and discharge process. Meanwhile, the conductive 3D CNT network realizes continuous electron/ion transport pathways and increases the contact area with the electrolyte. As a cathode for SIBs, the NVPF@CNTs displays superior Na$^+$-storage performance.

Experimental section

Synthesis method

Twenty-milligram carbon nanotubes were dispersed in 40 mL deionized water with untrasonication for 20 min. One-gram carbamide was added into the above solution under magnetic stirring for 20 min. The mixed solution was transferred to a 50 mL PTFE-lined autoclave and heated at 180 °C for 8 h. After washing three times with distilled water and ethanol, the powders were dried at 60 °C for 12 h. 5 mmol NH_4VO_3, 5 mmol $(NH_4)_2HPO_4$, 7.5 mmol NaF, and 2.5 mmol Na_2CO_3 were dissolved in 50 mL deionized water under magnetic stirring at 80 °C until the solution appeared orange (marked as solution A). The treated carbon nanotubes were added into a 50 mL PTFE-lined autoclave with 10 mL solution A and 20 mL DMF, then the autoclave was heated at 180 °C for 20 h. After washing with distilled water and ethanol, the precipitate was dried at 80 °C for 12 h. Subsequently, the sample was calcined at 400 °C for 1 h under Ar atmosphere to obtain the carbon nanotube composite NVPF (marked as NVPF@CNTs). The bare NVPF is synthesized by similar routes without adding carbon nanotubes (notated as NVPF).

Structural characterization

The structure of NVPF and NVPF@CNTs was characterized by powder X-ray diffraction (D8 Advance, Cu Kα radiation). The morphologies were examined by transmission electron microscope (TEM, JEOL-2100) and field-emission scanning electron microscope (FESEM, JSM-7500F). X-ray photoelectron spectra were acquired from an ESCALAB 250 system. Each spectrum was calibrated using the C1s binding

energy at 284.6 eV. Thermogravimetric analysis (TGA) was tested on a Mettler Toledo TGA/SDTA851 thermal analyzer at a heating rate of 10 °C min^{-1} in N_2 atmosphere. Raman spectrum was performed using a NEXUS 670 FT-IR Raman spectrometer.

Electrochemical measurements

The working electrodes were prepared with 70 wt% of active material (NVPF and NVPF/C powders), 20 wt% of acetylene black, and 10 wt% of polyvinylidene fluoride binder (PVDF). The mixture was pasted onto an Al foil and dried in a vacuum oven at 80 °C for 12 h. The loading mass of active material was about 0.9–1.1 mg cm^{-2}. The NaClO$_4$ solution (1 mol L^{-1}) in EC-DEC (1:1 volume) with 2% FEC solution was used as the electrolyte, while the glass fiber membrane (Whatman GF/D) was used as separator. The cells were tested in the voltage range of 2.0–4.2 V by using Land CT2001A battery testing system. The cyclic voltammetry (CV) was carried out with a CHI 760E electrochemical workstation. The capacity was calculated by the whole material. The current interruption method was measured in the voltage range of 2.0–4.2 V when the cell was cycled to 50 cycles. In the process of charge and discharge, the current was reduced to 0 in several preset charge states or discharge depth, and then stood for 18 s. Electrochemical impedance spectra (EIS) were conducted on an Autolab PGSTAT302N electrochemical workstation. It has been carried out between 100 kHz and 0.1 Hz at 2 V vs. Na/Na$^+$ after 3 cycles.

Results and discussions

To identify the effect of CNTs on the structure of NVPF, the XRD measurement of NVPF and NVPF@CNTs are displayed in Fig. 1A. The sharp peaks in the patterns indicate that NVPF and NVPF@CNTs are well crystalline. All of the diffraction peaks for them can be well assigned to the standard values of the JCPDS date (PDF#01–089-8485) [17–19]. The NVPF and NVPF@CNTs possess tetragonal structure with space group of $P4_2/mnm$ and there is no obvious difference between the two samples [20–23]. It is indicated the CNTs are rare impact to the crystal structure of NVPF. There are no obvious peaks of carbon in the XRD patterns, suggesting that the residual carbon in NVPF might be amorphous. The peak of CNTs at 26° coincides with the peak of NVPF at the same position. This phenomenon can also be verified from the literature reports [15, 16, 24]. In order to evaluate the vanadium oxidation state of NVPF@ CNTs, XPS spectrum was conducted (Fig. 1B). The spectra of V2p in NVPF@CNTs is divided into two doublets of V 2p$_{1/2}$ and V 2p$_{3/2}$ from V^{4+} and V^{3+}. The V 2p$_{3/2}$ peak centered at binding energies 516.3 and 515.1 eV which
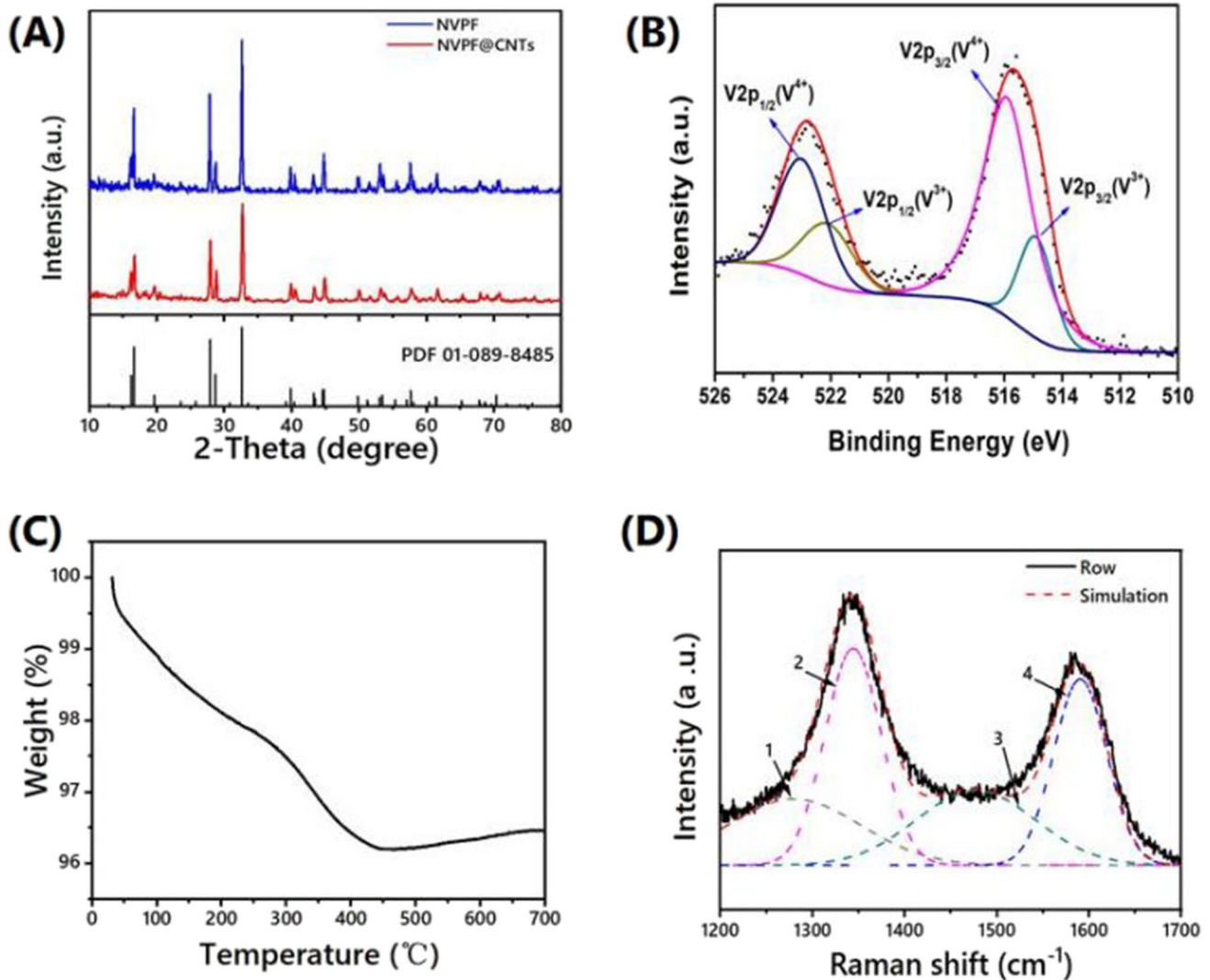
Fig. 1 **A** The XRD patterns of NVPF and NVPF@CNTs; **C** the XPS curve of NVPF@CNTs; **B** the TG curve and **D** Raman spectrum of NVPF@CNTs

are characteristics of V^{4+} and V^{3+}, respectively. The weak binding energies at 523.5 and 522.2 eV could be attributed to V $2p_{1/2}$ of V^{4+} and V^{3+}, respectively [25, 26], confirming the mixed V^{3+}/V^{4+} valence state and in agreement with Rietveld analysis of the XRD diffraction data (Fig. S1). The lattice parameters of $a = 9.0562(1)$ Å, $b = 9.0562(1)$ Å, and $c = 10.6559(4)$ Å (Rp: 3.60%, Rwp: 4.13%, χ^2: 1.91) suggest that the chemical composition of NVPF is the solid solution $Na_3V_2(PO_4)_2F_{2.9}O_{0.1}$ [20, 21]. The amount of CNTs in the NVPF@CNTs is about 2.9 wt%, determined by TGA measurement, as shown in Fig. 1C. The Raman spectra are performed to further investigate the state of carbon in the NVPF@CNTs composite (Fig. 1D). The two typical Raman signals (D band of 1330 cm^{-1} and G band of 1590 cm^{-1}) can be observed. The D band is attributed to disordered carbon and the G band is ascribed to crystalline graphitized carbon

[27–29]. The relative intensity ratio of I_D/I_G is usually a criterion to assess the degree of the disorder or the defects in the carbon structure [30, 31]. The I_D/I_G value in our work is fitted to 0.996. It is suggested the structural disorder degree is relatively low in the NVPF@CNTs structure and the CNT framework has a good crystallinity, leading to a high electronic conductivity.

Figure 2 shows the morphology of NVPF and NVPF@CNTs. The pure NVPF presents uniform microsphere-like structure with the size of 1~2 μm (Fig. 2A). It can be seen from SEM image that the microspheres are constituted by nanoparticles (Fig. 2B). When CNTs were added, as displayed in Fig. 2C, D, the NVPF microspheres are wrapped by the CNTs. The size of microspheres for NVPF@CNTs is lower than that for pure NVPF and some spheres fall to pieces. The size of these pieces is about 200 nm. It is

Fig. 2 The TEM images and SEM images of **A**, **B** NVPF and **C**, **D** NVPF@CNTs
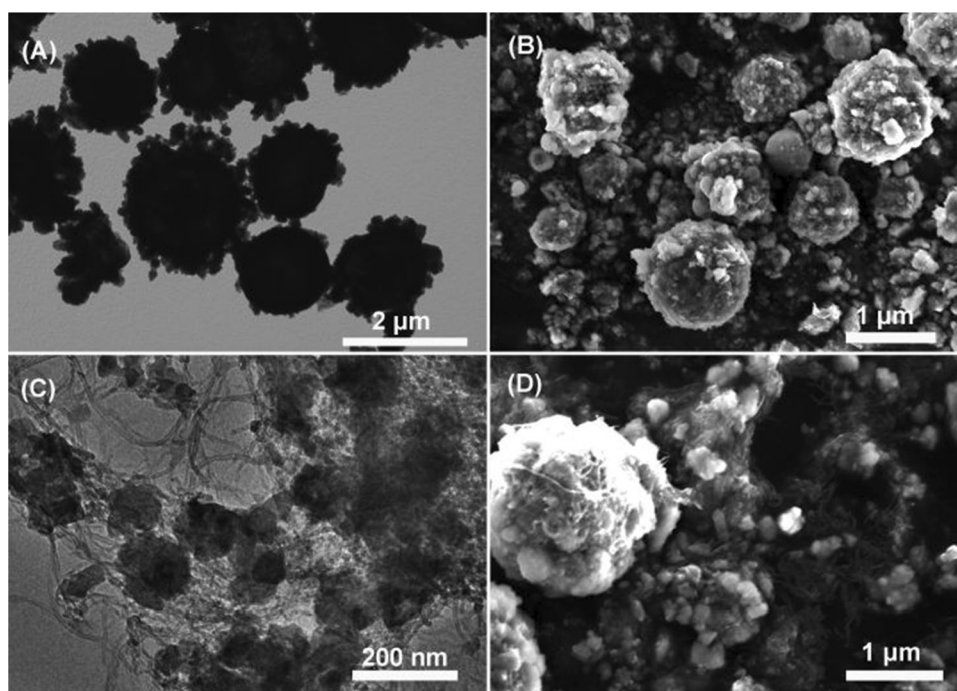
indicated that the introduction of the CNTs can effectively limit the growth of NVPF microspheres. This unique architecture with 3D conductive network is conducive to improvement of electrical conductivity for NVPF and buffers the change of volume caused by repeated extraction/insertion of Na$^+$ [4, 15, 16]. In Fig. S2, a typical HRTEM image of NVPF@CNTs shows a clear and continuous lattice fringe with an interplanar spacing of 0.53 nm, corresponding to the (002) crystal plane. There are no obvious amorphous layers in the HRTEM image, suggesting that the residual carbon in NVPF might be amorphous.

In order to evaluate the electrochemical performance of NVPF and NVPF@CNTs, charge and discharge profiles for the 1st, 10th, and 100th in the voltage range of 2.0–4.2 V at 0.2 C are shown in Fig. 3A and B (1 C = 128 mA g^{-1}). Two pairs of redox plateaus at the potential of about 3.47/3.71 V and 3.95/4.19 V were observed in the charge/discharge curves of both cathodes, corresponding to the redox reaction of V^{4+}/V^{3+} with extraction/insertion of two Na$^+$. In addition, the gap between charge and discharge plateaus of NVPF@CNTs electrode is narrower than that of NVPF, suggesting the rapid Na$^+$ extraction/insertion and enhanced redox kinetics. As displayed in Fig. 3C, NVPF@CNTs displays higher discharge capacity than that of pure NVPF, with a stable discharge capacity of 117 mAh g^{-1} after 300 cycles at a rate of 0.2 C. The rate performances of NVPF and NVPF@CNTs were measured at consecutive current densities varied from 0.1 C to 5 C (Fig. 3D). The NVPF@CNTs delivers reversible capacities of 130, 119.2, 114.2, 107.7, and 97.9 mA h g^{-1} at current densities of 0.1, 0.2, 0.5, 1, and

2 C, respectively, which is much better than that of NVPF. In particular, the high discharge capacity of 80.1 mAh g^{-1} can be remained even at a high current density of 5 C for NVPF@CNTs. Obviously, when the current density returns to 0.2 C, the specific capacity recovers to 116.2 mAh g^{-1}, indicating an excellent reversibility. The rate performance is inferior, indicating that the introduction of carbon will benefit the good use of positive active material. Subsequently, the ultrastable long-term cyclability of NVPF@CNTs was also measured (Fig. 3E). The reversible capacity of 73.4 mAh g^{-1} can be maintained with excellent capacity retention of 91.6% even after 600 cycles. In addition, the NVPF@CNTs as cathode for a single cointype battery enable to light up 21 diode bulbs (inset of Fig. 3E). The excellent electrochemical performance of NVPF@CNTs can be attributed to its 3D conduction network and a firm mechanical backbone framework for carbon nanotube, as well as the nanoscale sphere morphology, which enables fast diffusion for Na$^+$. In order to study the electrochemical behavior and kinetic reaction process of the samples, the electrochemical impedance spectroscopy of NVPF and NVPF@CNTs were further tested, as shown in Fig. 3F. It has been carried out between 100 kHz and 0.1 Hz at 2 V vs. Na/Na$^+$ after 3 cycles. The simulated charge transfer resistance (R_{ct}) of NVPF@CNTs shows 318 Ω, which is much lower than that of NVPF (R_{ct} = 436 Ω), suggesting that the CNTs are beneficial to improve the charge transfer of Na$^+$ from the electrolyte to active material.

To investigate the kinetic behavior of the NVPF@CNTs, the CV curves are obtained at different scanning rates ranging from 0.1 to 0.5 mV s^{-1} in the potential range
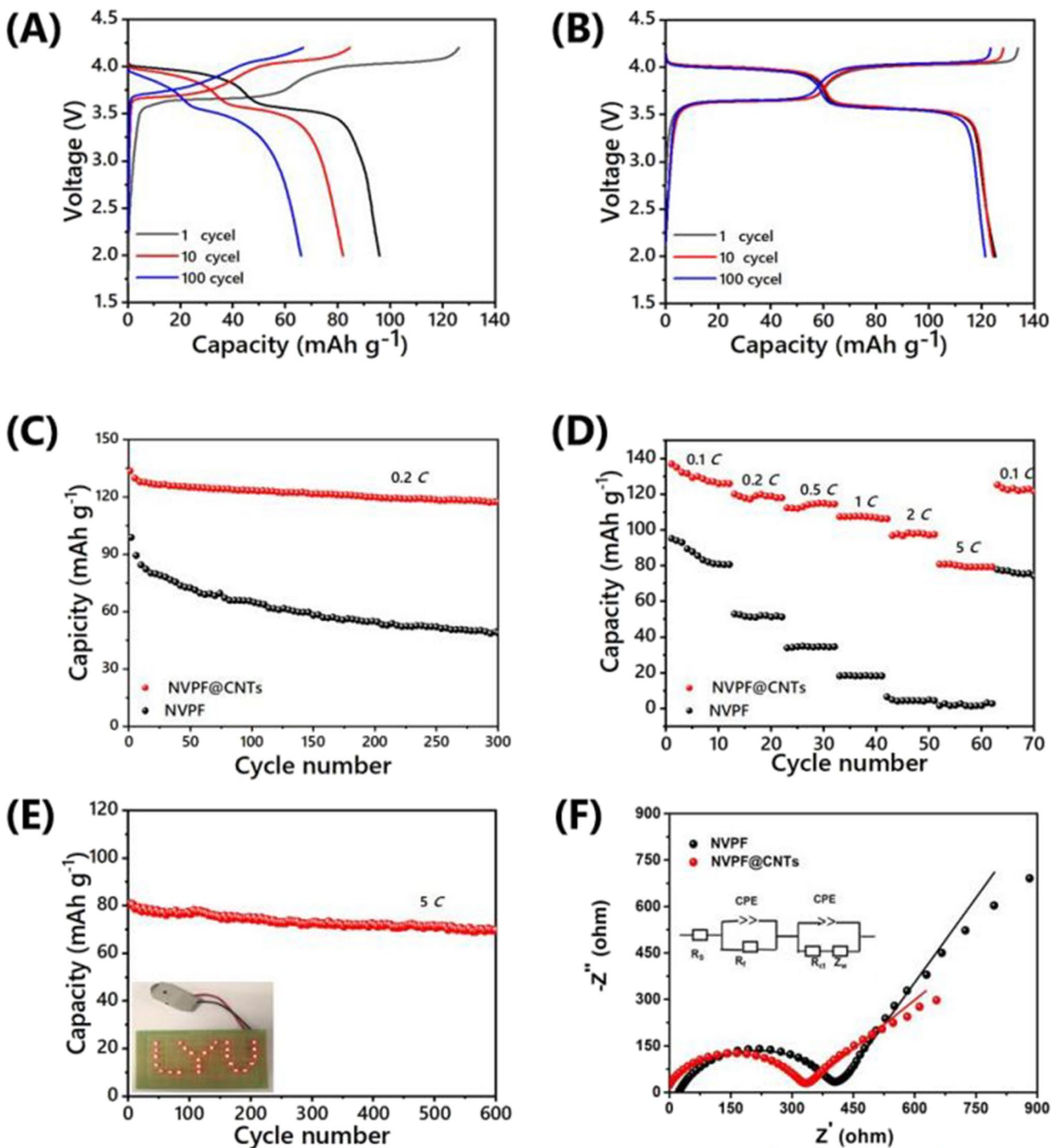
Fig. 3 A, **B** The charge–discharge curves of NVPF and NVPF@ CNTs; **C** cycling performances at 0.2 *C* of NVPF and NVPF@CNTs; **D** rate capabilities of NVPF and NVPF@CNTs; **E** long-term cycling performance of NVPF@CNTs at 5 *C*; **F** the Nyquist plots of the impedance spectra of NVPF and NVPF@CNTs (inset is an equivalent circuit)

between 2 and 4.5 V vs. Na⁺/Na. The height and the area of the CV curve increase with the scan rate increases. The diffusion behavior or the capacitance behavior of the battery can be calculated on the basis of Eq. (1):

$$i_p = av^b \tag{1}$$

where i_p is the peak current, v is the scan rate, and a and b are adjustable values [32, 33]. As shown in Fig. 4B, the
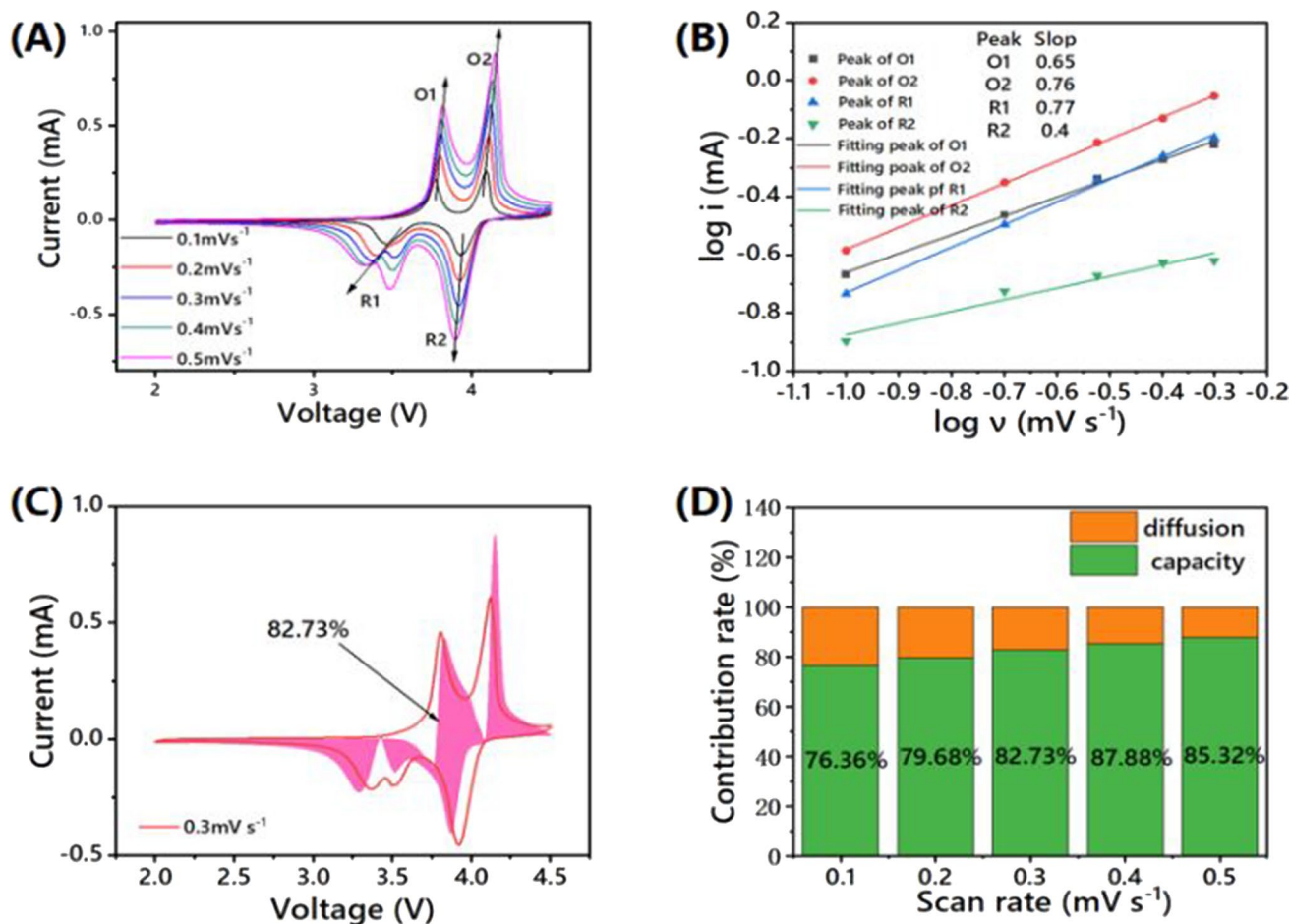
Fig. 4 **A** CV curves at various scan rates; **B** the fitted lines of $\log i_p$ vs. $\log v$; **C** the separation of the capacitive and diffusion currents at a scan rate of 0.3 mV s^{-1}; **D** the contribution of diffusion-controlled capacity (orange) and pseudocapacitive-controlled capacity (green) at different scan rates

b values corresponding to the O_1, O_2, R_1, and R_2 can be calculated to be 0.65, 0.76, 0.77, and 0.40, respectively. It is suggested that the pseudocapacitive effect predominates throughout the electrochemical process. The specific contribution of pseudocapacitance behavior can be further quantified according to formula (2):

$$i(V) = k_1 v + k_2 v^{1/2} \tag{2}$$

where v is the scan rate, V is the specified voltage, and k_1 and k_2 are parameters. Meanwhile, $k_1 v$ and $k_2 v^{1/2}$ represent the pseudocapacitance-controlled and diffusion-controlled behavior, respectively [34, 35]. As demonstrated in Fig. 4C, the contribution of the pseudocapacitive-controlled capacity is 82.73% according to the middle pink area. Meanwhile, in the range of scan rates from 0.1 mV s^{-1} to 0.5 mV s^{-1}, the pseudocapacitance contribution ratio is 76.36%, 79.68%, 82.73%, 87.88%, and 85.32%, respectively (Fig. 4D).

To further clarify the kinetic behavior for Na intercalation/extraction processes, DC resistance of NVPF and NVPF@CNTs has been recorded in Fig. 5. The DC resistance was measured by using current pulse technique after 50 charge/discharge cycles (Fig. 5A and B). After calculation based on the current pulse technique, the DC resistance of the NVPF@CNTs electrode is smaller than that of NVPF no matter in charge state or discharge state, which is lower than 2×10^3 Ω. It is boldly concluded that the addition of CNTs may change the microstructure of NVPF@CNTs and effectively reduce the contact resistance, then increase the diffusion of Na ions.

In situ XRD method was utilized at various voltage states to reveal the charged/discharged mechanism of NVPF@CNTs. The data was collected every 15 min at 0.2 C rate in the first two charge/discharge cycles. All the evolution of crystal structure was shown by the 3D color mode of
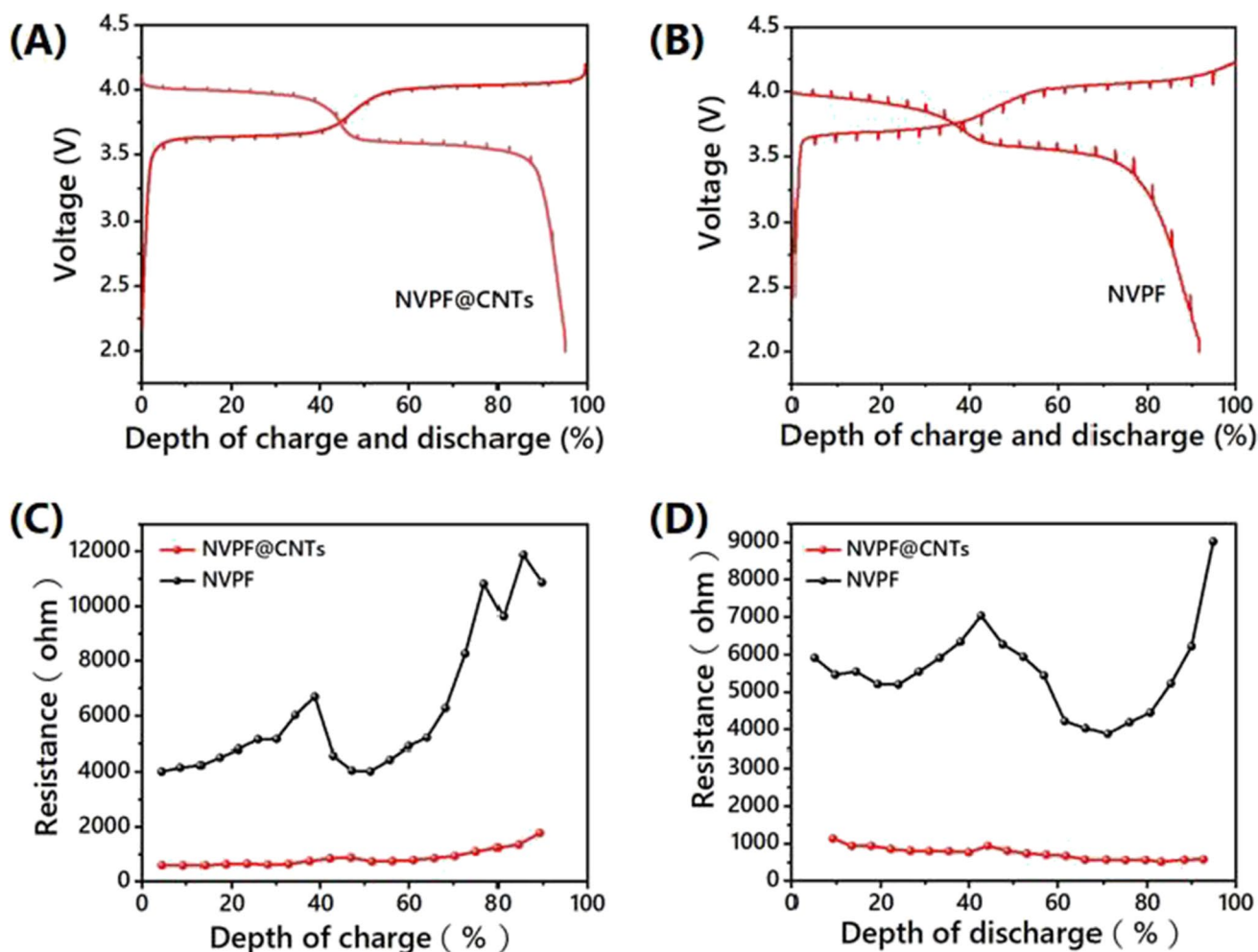
Fig. 5 **A** The charge curves and **B** the discharge curves of NVPF@ CNTs and NVPF using the current interruption test method when cycled to 50 cycles; **C** the relationship between the DC resistance of NVPF@CNTs and NVPF and the state of charge depth; **D** the relationship between the DC resistance of NVPF@CNTs and NVPF and the state of discharge depth

in situ XRD performed in the range of 10–65°. Due to the low content of the CNFs, the XRD peaks of carbon-based materials are undetectable. Therefore, in situ XRD patterns of the NVPF@CNTs only represent structural evolutions of the NVPF. As demonstrated in Fig. 6, the 2θ angle of 28° and 33° belonging to the (220) and (222), respectively, shift to the high angle. The peak of 28° gradually converges at 29° with the (103) planes and the peak of 29° shifts to lower degrees as the voltage charges to 4.2 V. It also can be observed no diffraction peaks disappear nor new peaks appear, suggesting the characteristics of a solid solution reaction [29, 36, 37]. Subsequently, all the diffraction peaks can be well recovered by discharging to 2.0 V from 4.2 V. These results indicate that the NVPF@CNTs has a highly reversible crystal structure in the process of Na⁺ extraction/ insertion. Based on the above results, the NVPF@CNTs composite with excellent electrochemical performance is a promising cathode material for SIBs on account of the

enhanced electron conductivity, good reaction kinetics, and unique architecture by cross-linked 3D CNT-wrapped NVPF.
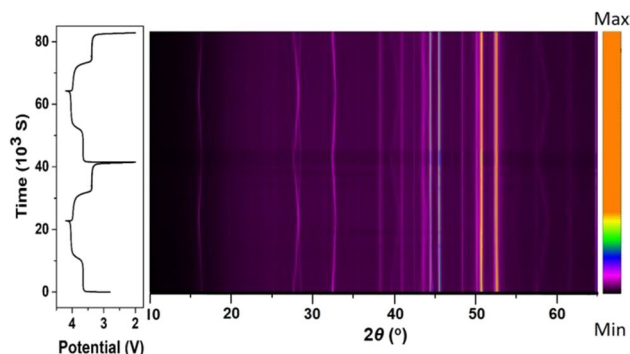

Fig. 6 3D color patterns of in situ XRD collected for the NVPF@ CNTs electrode during two successive cycles at a 0.2 *C* rate and the corresponding galvanostatic charge/discharge curve

Conclusions

In conclusion, we proposed a solvothermal method and subsequent heat treatment to construct a 3D composite structure of CNT-intertwined NVPF nanospheres. The NVPF@CNTs as cathode for SIBs displays a specific capacity of 117.6 mAh g^{-1} at 0.2 C after 300 cycles. When measured at 5 C, NVPF@CNTs electrode exhibits 73.4 mAh g^{-1} after 600 cycles with 91.6% of its initial discharge capacity. The different scanning rates of CV technology are utilized to illustrate that the pseudocapacitive effect predominates throughout the electrochemical process. The in situ XRD technique reveals that the electrochemical behavior of NVPF@CNTs is a reversible process of Na$^+$ extraction/insertion. We hope this work may accelerate the practical application of SIBs by hierarchical structure design.

References

1. Han MH, Gonzalo E, Singh G, Rojo T (2015) A comprehensive review of sodium layered oxides: powerful cathodes for Na-ion batteries. Energy Environ Sci 8:81

2. Ghosh S, Barman N, Mazumder M, Pati SK, Rousse G, Senguttuvan P (2020) High capacity and high-rate NASICON-Na$_{3.75}$V$_{1.25}$Mn$_{0.75}$(PO$_4$)$_3$ cathode for Na-ion batteries via modulating electronic and crystal structures. Adv Energy Mater 10:1902918

3. Chen Y, Cheng J, Sun S, Tian Z, Jiang X, Wang Y, He Z, Liu C, Huang Q, Guo L (2021) Constructing hierarchical porous Fe/F-codoped Na$_3$V$_2$(PO$_4$)$_3$/C composite enwrapped with carbon nanotubes as high-performance cathode for symmetric sodium ion batteries. J Power Sources 513:230545

4. Zhu L, Wang H, Sun D, Tang Y, Wang H (2020) A comprehensive review on the fabrication, modification and applications of Na$_3$V$_2$(PO4)$_2$F$_3$ cathodes. J Mater Chem A 8:21387–21407

5. Jin T, Li H, Zhu K, Wang PF, Liu P, Jiao L (2020) Polyanion-type cathode materials for sodium-ion batteries. Chem Soc Rev 49:2342

6. Sun S, Chen Y, Cheng J, Tian Z, Wang C, Wu G, Liu C, Wang Y, Guo L (2021) Constructing dimensional gradient structure of Na$_3$V$_2$(PO$_4$)$_3$/C@CNTs-WC by wolfram substitution for superior sodium storage. Chem Eng J 420:130453

7. Chen Y, Cheng J, Wang C, He Z, Wang Y, Li D, Guo L (2021) Simultaneous modified Na$_{2.9}$V$_{1.9}$Zr$_{0.1}$(PO$_4$)$_3$/C@rGO as a superior high rate and ultralong lifespan cathode for symmetric sodium ion batteries. Chem Eng J 413:127451

8. Wang J-H, Wang W-X, Du P, Hu F-D, Jiang X-L, Yang J (2019) Synthesis of Na$_3$V$_2$(PO$_4$)$_2$F$_3$@V$_2$O$_{5-x}$ as a cathode material for sodium-ion batteries. J Inorg Mater 34:1097

9. Deng L, Yu F-D, Xia Y, Jiang Y-S, Sui X-L, Zhao L, Meng X-H, Que L-F, Wang Z-B (2021) Stabilizing fluorine to achieve high-voltage and ultra-stable Na$_3$V$_2$(PO$_4$)$_2$F$_3$ cathode for sodium ion batteries. Nano Energy 82:105659

10. Hwang J, Matsumoto K, Hagiwara R (2020) Electrolytes toward high-voltage Na$_3$V$_2$(PO$_4$)$_2$F$_3$ positive electrode durable against temperature variation. Adv Energy Mater 10:2001880

11. Chen C, Li T, Tian H, Zou Y, Sun J (2019) Building highly stable and industrial NaVPO$_4$F/C as bipolar electrodes for high-rate symmetric rechargeable sodium-ion full batteries. J Mater Chem A 7:18451

12. Li X, Jiang S, Li S, Yao J, Zhao Y, Bashir T, Zhou S, Yang S, Li W, Zhu W, Liu T, Zhao J, Gao L (2021) Overcoming rate-determining kinetics of Na$_3$V$_2$O$_2$(PO$_4$)$_2$F cathode for ultrafast sodium storage by heterostructured dual-carbon decoration. J Mater Chem A 9:11827

13. Cai Y, Cao X, Luo Z, Fang G, Liu F, Zhou J, Pan A, Liang S (2018) Caging Na$_3$V$_2$(PO$_4$)$_2$F$_3$ microcubes in cross-linked graphene enabling ultrafast sodium storage and long-term cycling. Adv Sci 5:1800680

14. Du P, Mi K, Hu F, Jiang X, Wang D, Zheng X (2020) Hierarchical hollow microspheres Na$_3$V$_2$(PO$_4$)$_2$F$_3$C@rGO as high-performance cathode materials for sodium ion batteries. New J Chem 44:12985

15. Liu S, Wang L, Liu J, Zhou M, Nian Q, Feng Y, Tao Z, Shao L (2019) Na$_3$V$_2$(PO$_4$)$_2$F$_3$-SWCNT: a high voltage cathode for non-aqueous and aqueous sodium-ion batteries. J Mater Chem A 7:248

16. Guo H, Hu Y, Zhang X, Zhang R, Hou D, Sui Y, Wu L (2019) Facile one-step hydrothermal synthesis of Na$_3$V$_2$(PO$_4$)$_2$F$_3$@C/CNTs tetragonal micro-particles as high-performance cathode material for Na-ion batteries. Front Chem 7:689

17. Hu F, Jiang X (2021) Superior performance of carbon modified Na$_3$V$_2$(PO$_4$)$_2$F$_3$ cathode material for sodium-ion batteries. Inorg Chem Commun 129:108653

18. Gu Z-Y, Guo J-Z, Sun Z-H, Zhao X-X, Wang X-T, Liang H-J, Zhao B, Li W-H, Pan X-M, Wu X-L (2021) Aliovalent-Ion-Induced Lattice Regulation Based on Charge Balance Theory: Advanced Fluorophosphate Cathode for Sodium-Ion Full Batteries. Small 17:2102010

19. Li L, Zhang N, Su Y, Zhao J, Song Z, Qian D, Wu H, Tahir M, Saeed A, Ding S (2021) Fluorine Dissolution-Induced Capacity Degradation for Fluorophosphate-Based Cathode Materials. ACS Appl Mater Interfaces 13:23787

20. Nguyen L, Broux T, Camacho PS, Denux D, Bourgeois L, Belin S, Iadecola A, Fauth F, Carlier D, Olchowka J, Masquelier C, Croguennec L (2019) Stability in water and electrochemical properties of the Na3V2(PO4)2F3 – Na3(VO)2(PO4)2F solid solution. Energy Storage Mater 20:324–334

21. Olchowka J, Nguyen L, Broux T, Camacho PS, Petit E, Fauth F, Carlier D, Masquelier C, Croguennec L (2019) Aluminum substitution for vanadium in the Na$_3$V$_2$(PO$_4$)$_2$F$_3$ and Na$_3$V$_2$(PO$_4$)$_2$FO$_2$ type materials. Chem Commun 55:11719–11722

22. Nguyen L, Camacho PS, Broux T, Olchowka J, Masquelier C, Croguennec L, Carlier D (2019) Density functional theory-assisted ^{31}P and ^{23}Na magic-angle spinning nuclear magnetic resonance study of the Na$_3$V$_2$(PO$_4$)$_2$F$_3$–Na$_3$V$_2$(PO$_4$)$_2$FO$_2$ solid solution: unraveling its local and electronic structures. Chem Mater 31:9759–9768

23. Fang R, Olchowka J, Pablos C, Camacho PS, Carlier D, Croguennec L, Cassaignon S (2022) Effect of the particles morphology on the electrochemical performance of Na$_3$V$_2$(PO$_4$)$_2$F$_{3-y}$O$_y$. Batter Supercaps 5:e202100179

24. Xie XQ, Zhao M-Q, Anasori B, Maleski K, Ren CE, Li JW, Byles BW, Pomerantseva E, Wang GX, Gogotsi Y (2016) Porous heterostructured MXene/carbon nanotube composite paper with high volumetric capacity for sodium-based energy storage devices. Nano Energy 26:513

25. Aragón M, Lavela P, Ortiz GF, Alcántara R, Tirado J (2017) Induced rate performance enhancement in off-stoichiometric $Na_{3+3x}V_{2-x}(PO_4)_3$ with potential applicability as the cathode for sodium-ion batteries. Chem-Eur J 23:7345–7352

26. Klee R, Aragón M, Lavela P, Alcántara R, Tirado J (2016) $Na_3V_2(PO_4)_3$/C nanorods with improved electrode-electrolyte interface ss cathode material for sodium-ion batteries. ACS Appl Mater Interfaces 8:23151–23159

27. Liang L, Li X, Zhao F, Zhang J, Liu Y, Hou L, Yuan C (2021) Construction and operating mechanism of high-rate Mo-doped $Na_3V_2(PO_4)_3$@C nanowires toward practicable wide-temperature-tolerance Na-ion and hybrid Li/Na-ion batteries. Adv Energy Mater 11:2100287

28. Li L, Xu YL, Sun XF, He SN, Li L (2018) High capacity-favorable tap density cathode material based on three-dimensional carbonous framework supported Na3V2(PO4)2F3 nanoparticles. Chem Eng J 331:712

29. Guo JZ, Wang PF, Wu XL, Zhang XH, Yan QY, Chen H, Zhang JP, Guo YG (2017) High-Energy/Power and Low-Temperature Cathode for Sodium-Ion Batteries: In Situ XRD Study and Superior Full-Cell Performance. Adv Mater 29:1701968

30. Criado A, Lavela P, Ortiz G, Tirado J, Gzouli S, Edfouf Zand Pérez-Vicente C (2019) CTAB-assisted synthesis of C@ $Na_3V_2(PO_4)_2F_3$ with optimized morphology for application as cathode material for Na-ion batteries. Front Phys 7:207

31. Criado A, Lavela P, Ortiz G, Tirado JL, Pérez-Vicente C, Bahrou N, Edfouf Z (2020) Highly dispersed oleic-induced nanometric C@$Na_3V_2(PO_4)_2F_3$ composites for efficient Na-ion batteries. Electrochim Acta 332:135502

32. Niu H, Yang Q, Wang Q, Jing X, Zhu K, Ye K, Wang G, Cao D, Yan J (2020) Oxygen vacancies-enriched sub-7 nm cross-linked $Bi_{2.88}Fe_5O_{12-x}$ nanoparticles anchored MXene for electrochemical energy storage with high volumetric performances. Nano Energy 78:105360

33. Zhang ZB, Chen ZH, Mai ZX, Peng KY, Deng QL, Bayaguud A, Zhao P, Fu YP, Yu Y, Zhu CB (2019) Toward high power-high energy sodium cathodes: a case study of bicontinuous ordered network of 3D porous $Na_3(VO)_2(PO_4)_2F$/rGO with pseudocapacitance effect. Small 15:1900356

34. Pu X, Zhao D, Fu C, Chen Z, Cao S, Wang C, Cao Y (2021) Understanding and calibration of charge storage mechanism in cyclic voltammetry curves. Angew Chem Int Edit 60:21310

35. Yang X, Wang Q, Zhu K, Ye K, Wang G, Cao D, Yan J (2021) 3D Porous Oxidation-Resistant MXene/Graphene Architectures Induced by In Situ Zinc Template toward High-Performance Supercapacitors. Adv Funct Mater 31:2101087

36. Shen X, Zhou Q, Han M, Qi X, Li B, Zhang Q, Zhao J, Yang C, Liu Ha, Hu Y-S (2021) Rapid mechanochemical synthesis of polyanionic cathode with improved electrochemical performance for Na-ion batteries. Nat Commun 12:2848

37. Qi Y, Mu L, Zhao J, Hu Y-S, Liu H, Dai S (2015) Superior Na-storage performance of low-temperature-synthesized $Na_3(VO_{1-x}PO_4)_2F_{1+2x}$ ($0 \leq x \leq 1$) nanoparticles for Na-ion batteries. Angew Chem Int Edit 54:9911